New detector concept with neutron interaction localization capabilities

J. Heideman[a], D. Pérez-Loureiro[a], R. Grzywacz[a,c,*], J. Chen[a], L. H. Heilbronn[b], S. K. Neupane[a], K. Schmitt[a,1], C. R. Thornsberry[a], M. M. Rajabali[d], A. R. Engelhardt[d], C. W. Howell[d], L. D. Mostella[d], J. S. Owens[d], S. C. Shadrick[d], E. E. Peters[f], A. P. D. Ramirez[f], S. W. Yates[f], S. Munoz[e]

[a]*Department of Physics and Astronomy, University of Tennessee, Knoxville, Tennessee , 37996 USA*
[b]*Department of Nuclear Engineering, University of Tennessee, Knoxville, Tennessee , 37996 USA*
[c]*Physics Division, Oak Ridge National Laboratory, Oak Ridge TN 37831 USA*
[d]*Department of Physics Tennessee Technological University, Cookeville, Tennessee, 38505, USA*
[e]*Joint Institute for Nuclear Physics and Applications, Oak Ridge TN 37831 USA*
[f]*Department of Physics and Astronomy and Chemistry, University of Kentucky, Lexington, Kentucky, 40506 USA*

Abstract

A new high precision time of flight neutron detector concept for beta-delayed neutron emission and direct reaction studies is proposed. The Neutron dEtector with Xn Tracking (NEXT) array aims to maintain high instrinsic neutron detection efficiency while reducing uncertainties in neutron energy measurements. A single NEXT module will be composed of thin segments of neutron-discriminating plastic scintillator, each optically separated, coupled to a position sensitive photo-detector. By incorporating a position sensitive photo-detector with a large optically separated scintillator, NEXT will achieve high precision determination of neutron time of arrival and interaction position within the active volume. A design study has been conducted based on simulations and experimental tests leading to construction of prototype units. First results from neutron measurements will be discussed.

Keywords: β-delayed neutron emission, direct reactions, time of flight

1. Introduction

New generation radioactive ion beam facilities enable access to very neutron rich nuclei, approaching, and even reaching the neutron drip-line in certain cases [1]. Far from stability, neutron separation energies decrease as beta-decay endpoint energies become large, increasing the likelihood of beta-delayed neutron emission. Neutron spectroscopy becomes essential to obtain important information about the nuclear structure for these very neutron-rich nuclei [2, 3, 4]. Neutron dEtector with Xn Tracking (NEXT) has been devoloped to observe beta-delayed neutron emitters with improved precision. These improvements will also be applicable to proton transfer reactions which probe discrete states of exotic nuclei. NEXT has been designed around neutron-gamma discriminating scintillator in order to improve background rejection. Prevelant gamma-ray background common in decay and reaction experimental setups can be reduced significantly in neutron spectra, further improving neutron energy measurements [5]. Proof of principle tests for the NEXT design study will be shown in this paper along with results from first neutron measurements.

2. Detector Design

When the neutron kinetic energies are measured via time-of-flight (ToF), the energy resolution is given by the following expression [6]:

$$\frac{\Delta E}{E} = \sqrt{\left(\frac{2\Delta t}{t}\right)^2 + \left(\frac{2\Delta L}{L}\right)^2}, \qquad (1)$$

in which t is the time-of-flight of the particle (Δt is uncertainty in time-of-flight) and L is the corresponding flight path-length (ΔL is the uncertainty

*Corresponding author
Email addresses: jheidema@vols.utk.edu (J. Heideman), rgrzywac@utk.edu (R. Grzywacz)
[1]Present address: Los Alamos National Laboratory, Los Alamos, New Mexico 87545, USA

in neutron path-length). Therefore, the energy resolution is directly related to the time resolution of the detection system, and the precision in the measurement of the path-length. The latter is mainly due the the uncertainty in the determination of the interaction point within the active volume of the detector. One of the factors which limits this precision is the required thickness along the trajectory, because the interaction can occur anywhere within the detector. Thick detectors are needed to maintain neutron detection efficiency, but at the expense of a good position resolution. Typical thicknesses for plastic-scintillator-based neutron ToF detectors are about 2-3 cm, which is a good trade-off between position resolution and efficiency [7, 8, 9, 10].

Common plastic scintillators exhibit the same response from gamma-ray scattering as neutron scattering, making the two events indiscernible. In order to correct this behavior, many types of neutron-gamma discriminating scintillators have been developed to improve gamma-ray background rejection in neutron time of flight distributions. By implementing neutron-gamma discriminating plastic, energy calculations can be further improved with increased background rejection using conventional pulse shape discrimination methods.

2.0.1. Detector Requirements

The design of the NEXT module is dictated by the necessity to obtain highest possible precision in measurement of position and timing of the neutron and the capabilities of the scintillator material and sensor. The optimal, realistic segmentation has to warrant sufficiently good light collection in order to retain timing and PSD capabilities. Figure 1 shows the dependencies of the neutron energy resolution on the thickness and timing resolution resulting from implementation of Equation 1 for a 1 m neutron flight path. The black curves in Figure 1 (a) and (b) represents current VANDLE capabilities [7] and shows the uncertainty in the ToF distance is the main limitation in the energy resolution of this detector, especially at neutron energies above 2 MeV.

It is apparent that, for a given $\frac{\Delta L}{L}$, the $\frac{\Delta t}{t}$ should be commensurate, meaning that for a particular timing resolution Δt, and particular L, there is an minimal segment thickness $\frac{\Delta L}{L}$, beyond which the timing resolution dominates the overall energy resolution. For the typical L=50-100 cm and Δt=1 ns timing resolution, the segment thickness should be no more than 10 mm. Thin detectors (3-6 mm)

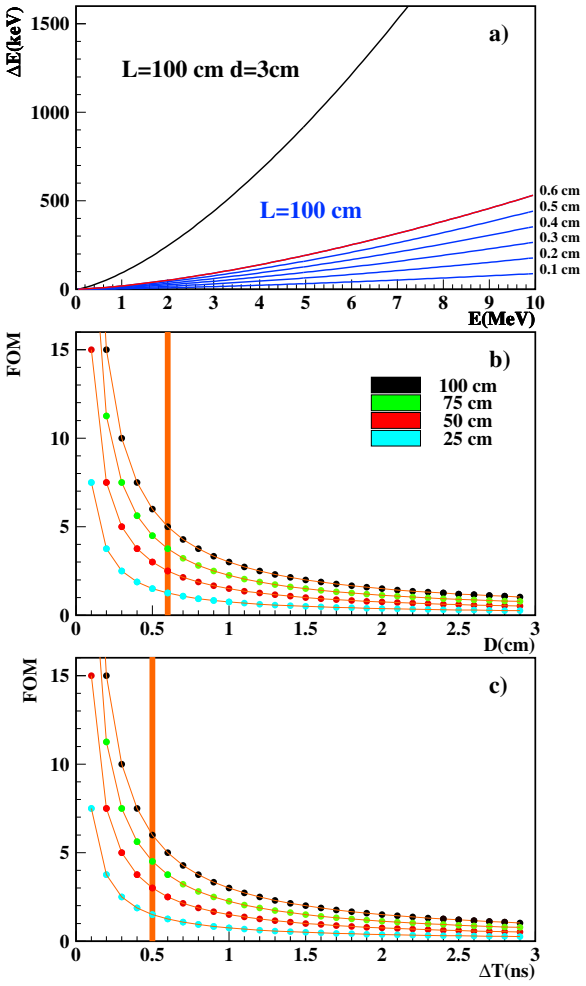

Figure 1: (a) Energy resolution of varying prototype tile thicknesses (1-6 mm) as a function of neutron energy. The black curve represents the current energy resolution calculations as a function of energy for a VANDLE (L=100 cm, ΔL=3 cm, and Δt=3 ns). (b) and (c) show Figure of Merit $\left(FOM = \frac{\Delta E}{\Delta E_{VANDLE}}\right)$ calculations as a function of tile thickness and timing resolution respectively. The different colored data points correspond to different flight path lengths. In (b), the timing resolution has been fixed to 500 ps and in (c), the position resolution has been fixed to 6 mm. The orange vertical line in (b) and (c) are the expected detector performance with current proposed design specifications (ΔL=6 mm and Δt=500 ps).

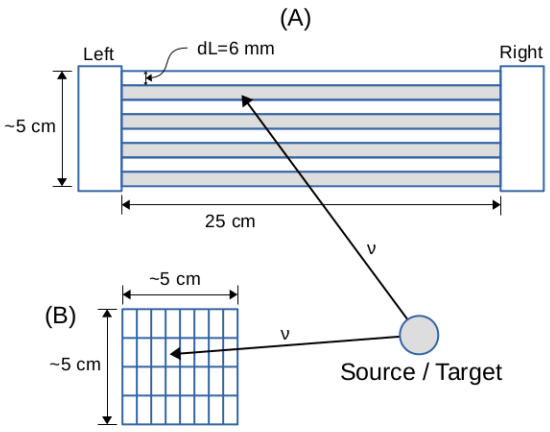

Figure 2: Schematic showing a potential detection configuration for a single NEXT module in a time-of-flight setup. (A) Shown is a top-down view of the detector segmentation along the neutron flight path. (B) Side view of a prototype showing the individual segements within the detector, each optically seperated from one another.

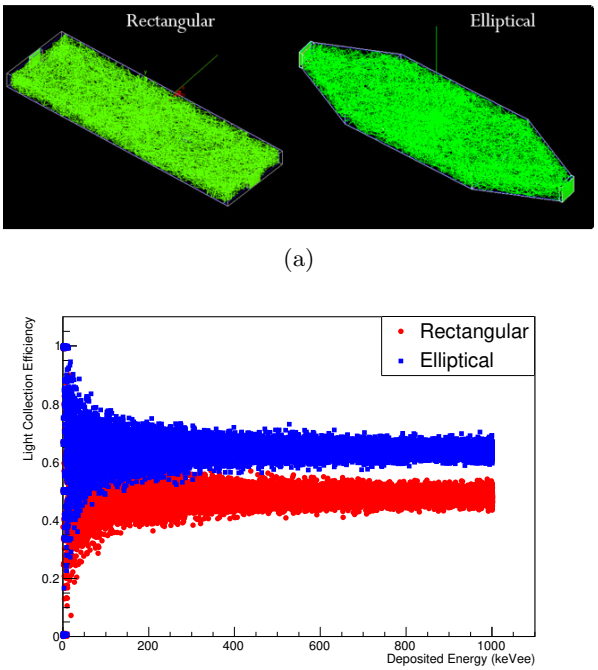

Figure 3: Visualization of a 1 Mev neutron event in NEXT*sim* for two geometries considered for a NEXT layer. Green lines correspond to optical photons produced in the scintillation.

will have lower uncertainty in the determination of the position while the contribution due to the time resolution becomes more important.

NEXT will also have to discriminate neutrons from gamma-rays. Scattered gamma-rays present during an experiment can coincide with start signals, causing significant background in the neutron time-of-flight spectrum. There are several solid-state scintillators which can provide good neutron-gamma discrimination and timing, such as stilbene, anthracene, and para-terphenyl. Each of them presently cannot be used as a material for the proposed detector due to limited ability to be machined into a large segmented array. When a viable neutron-gamma discriminating plastic scintillator was first developed [11], the polymer was not rigid enough to facilitate machining. The plastic scintillator commercialized as Eljen 299 (EJ-299) had to be cast directly into the final detector geometry, making the assemby of a segmented detector from this plastic scintillator expensive and time consuming. However, recent improvements to the EJ-299 polymer matrix has increased physical stability as well as pulse shape discrimination capabilities [12]. This new plastic scintillator, Eljen 276 (EJ-276), has neutron-gamma discrimination comparable to liquid scintillator and is now rigid enough to be machined to the appropriate thicknesses for a high resolution neutron time-of-flight detector.

2.1. Detector Concept

The NEXT array concept is based on multi-layered modules of neutron-gamma discriminating plastic scintillator with a position sensitive photodetectors on both ends of a module. Each module consists of eight 6-mm-thick layers, therefore the total effective thickness is 4.8 cm. These dimensions were driven, among other factors, by the availability of small form factor photo-sensors and will be substantiated later in the text. Figure 2 shows a possible multi-layered module configuration, with segmentation along the horizontal and vertical directions. The photon sensors considered are either an array of silicon photomultipliers (SiPMs) or flat panel multi-anode photomultiplier tubes (MAPMTs). Analysis of the position sensitive photosensor response from detected scintillation light will determine the precise layer in which the neutron scattered, reducing the uncertainy in the neutron flight path-length. The fast timing (sub nanosecond) capabilities of these photosensors will further improve energy resolutions by reducing the time-of-flight uncertainty.

3. Simulations: NEXT*sim*

In order to investigate the light collection efficiency as well as the timing capabilites of the different considered geometries, *NEXTsim*, a GEANT4-based code was developed [13, 14]. The NEXT*sim* code uses GEANT4 version 10.1 Patch 3 and outputs to ROOT files for further analysis. The software simulates the interaction of neutrons, gammas, and charged particles in the matter they traverse. The physics model (referred as *Physics List* in the GEANT4 context) employed is the recommended QGS_BERT_HP, which includes the standard electromagnetic, and the high precision models for neutron scattering, elastic and inelastic, as well as capture and fission. This model is based on the G4NDL evaluated neutron data library [15]. In addition to this physics list, the G4OpticalPhysicsList is included to treat the transport of scintillation light as well as the G4RadioactiveDecay to simulate radioactive sources. The generation of the primary particles was made with the GeneralParticleSource (GPS) module, which allows to define complex beam profiles or source geometries. This module allows the user to define the primary particle, spacial and angular distribution, as well as the kinetic energy with simple commands.

Different geometries considered for NEXT modules can be modeled and simulated (see top picture in Figure 3), e.g. rectangular bars and elliptical bars (bars in which the corners were cut in angle to maximize the light focusing in the detector). The user can select between any of the geometries, scintillator, and wrapping materials via macro-driven commands.

For every event, the simulation tracks the incoming particle and registers each interaction in the different layers of matter and stores the information in a *ScintHit* object, which includes position, time and momentum. The collection of hits of each event is stored in a ROOT *TClonesArray* and then saved in a *Tree*.

In addition, the code is also able to simulate the scintillation process induced by the scattered particles within the detector volume. All the optical photons produced are then tracked until they are detected or absorbed. For each detected photon, their positions and arrival times are recorded in a *OptPhotonHit* and the hit collection is saved in the same *Tree* as the emphScintHits.

3.1. Simulation of light collection efficency

The different geometries considered for the NEXT detector were simulated in order to determine the light collection efficiency. Figure 3 shows the results of the light collection efficiency, calculated as the ratio between detected and produced photons, as a function of the energy deposited in the scintillator. In this case the photosensors are considered ideal and every photon hitting the sensitive surface will be detected. We observe that the rectangular geometries have efficiencies close to 50% on average. The efficiency of the elliptical shape is higher and it reaches up to 68% due to the focusing effect towards the photosensors.

3.2. Simulation of photosensor response

The signals produced by the scintillation light in the detectors were also added to the simulations. The Single Photo Electron (SPE) response function of the photosensors were folded with the optical photon distribution to obtain a realistic photomultiplier signal. The SPE functions for SiPMs and PMTs were taken from [16]. The total response is the sum of the SPEs of each photon arriving at the photo-sensor weighted by the gain of the anode which it struck. The resultant light-response pulse is then given a baseline, electrical noise, and is then "digitized" by placing it into discrete bins on the y-axis (e.g. from 0 to 65535 to represent a 16-bit digitizer) and discrete time bins on the x-axis (e.g. 4 ns for a 250 MSPS system). The digitized pulses are then integrated to obtain the representative light of the event and are processed with a polynomial constant fraction discrimination algorithm (PolyCFD) [17] as discussed in section 4.2. The PolyCFD algorithm computes a time for each pulse which represents the time-of-flight of the incident neutron aggregated from all collected photons.

3.3. Simulation of time of flight resolution of the detector

The time of flight spectrum of 1 MeV neutrons impinging onto 10-cm-long plastic scintillator bars was simulated in order to determine their timing resolution. Geometrical cross-sections of 6×6 mm^2, 3×3 mm^2, and 1×1 mm^2 were simulated in order to determine the effect of cell thickness on the measured time resolution. Photosensitive surfaces were used for each test. The absolute timing (first photon arrival) was used to measure the neutron

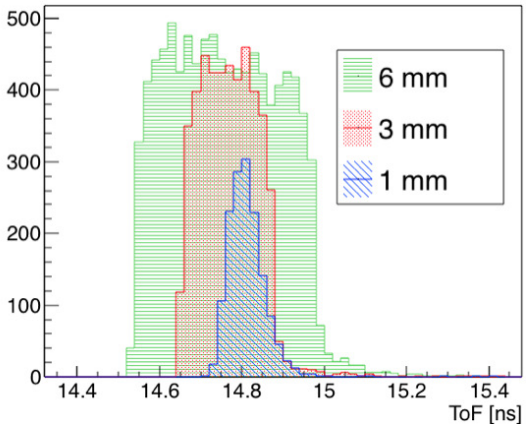

Figure 4: Distribution of the time of flight for a pencil beam placed 20 cm away from the detector of 1 MeV neutrons impinging onto scintillators of varying thickness.

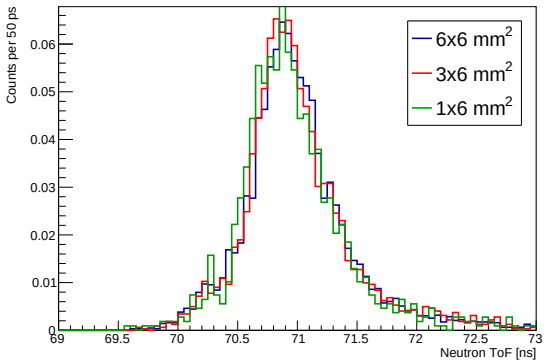

Figure 5: Distribution of the time of flight for a pencil beam of 1 MeV neutrons impinging on scintillator plates 1 m away. Normalized ToF distributions are shown for 10 cm plates with geometric cross-sections of 6×6 mm^2 (blue), 3×6 mm^2 (red), and 1×6 mm^2 (green).

time-of-flight in order to precisely determine the effect of the thickness of the bar. Figure 4 shows that an increase in the thickness of the scintillator bar results in an overall broadening of the time of flight resolution.

For another test, scintillator plates with cross-sections 6×6 mm^2, 3×6 mm^2, and 1×6 mm^2 and standard 6×6 mm^2 PMT sensitive surfaces on each end were bombarded with a pencil beam of 50,000 1 MeV neutrons traversing a distance of 1 m. The light output and timing of each PMT response is computed as in section 3.2 and the neutron time-of-flight (ToF) is computed as the average of the arrival time of the light pulse for the left and right PMTs. Figure 5 shows the normalized ToF distributions for each plate overlayed on one another. When the full data acquisition and analysis is taken into account, the ToF resolutions of the various plate widths are dominated by the overall acquisition time resolution. The FWHM time resolution for the three different plates are all within 5% of one another and average to approximately 583 ps for the beam of 1 MeV neutrons. The simulation also shows the detection efficiency of a plate scales linearly with its thickness (i.e. the efficiency of the 6×6 mm^2 plate is two times larger than the 3×6 mm^2 plate which, in turn, is three times larger than the 1×6 mm^2. This means that in addition to posessing six times greater efficiency, the 6×6 mm^2 plate exhibits approximately the same detector time resolution as the 1×6 mm^2 when coupled to a realistic acquistion.

Based on this result, it was decided that the minimum tile thickness of a prototype should not be less than 6 mm; thinner tiles would not provide any further benefit due to the timing resolution limit of the data acquisition system.

3.4. Study of neutron backscattering

Investigating neutron back scattering is very important in a multi-layered detector like NEXT. If a neutron is backscattered to a previous layer this may lead to a wrong determination of the neutron kinetic energy

The *NEXTsim* code was employed to evaluate the probability of backscattering in different layers of the detector after 2, 3 and 4 scattering events in the detectors for neutron energies between 100 keV and 5 MeV. The simulation tracks the neutron while traversing the detector layers and we count a backscattering event if the difference between the final and initial layers is negative. Figure 6 shows the result of the position difference in layers obtained the simulation for a 2 MeV neutron pencil beam. The probability of backscattering is lower than 5% after a single scatter and after several scatters within the detector volume the probability reaches below 12%.

Simulations of the NEXT prototype have shown that a position dependent time-of-flight neutron detector should be capabale of measuring neutrons with improved energy resolution. The NEXT prototyping process was guided by simulation results which minimized the effort needed to fully test every configuration with an experimental setup.

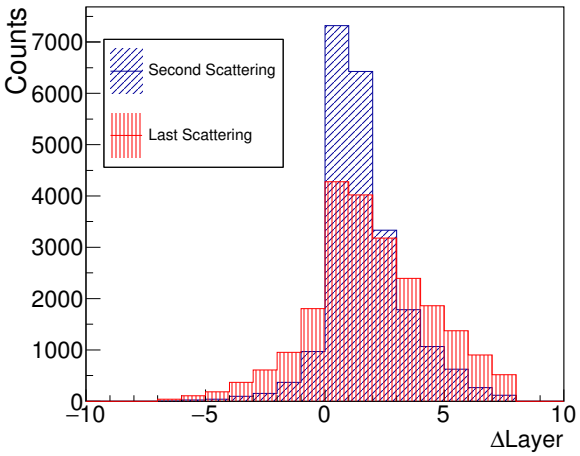

Figure 6: Layer difference between the second (blue) and last (red) scattering events within the NEXT detector for a 2 MeV incident neutron.

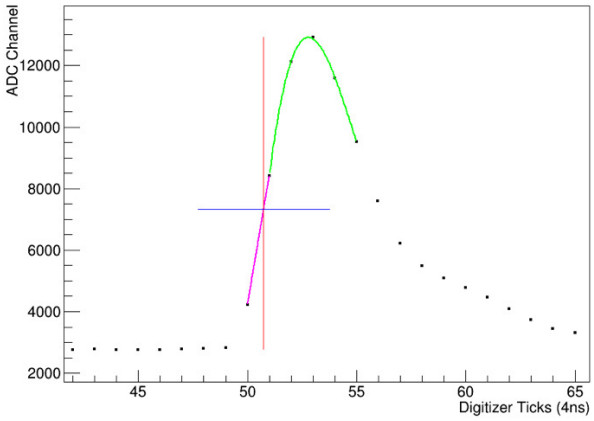

Figure 7: Example of the PolyCFD algorithm on a digitized trace. Green line represents the third order polynomial fit of the maximum. Magenta line shown the linear interpolation, and the blue line the threshold level. The high resolution time is determined by the intersection between the magenta and blue lines and it is represented by the red vertical line.

Going forward, the NEXTsim framework will be continually developed to provide first estimates of new detector capabilities and simulate state of the art experiments using full detector array configurations.

4. Detector Prototyping

The development phase of the NEXT project investigated single segment scintillator prototypes of various geometries and different photosensors. The key point of these tests was to explore whether the scintillation produced in the interaction of neutrons in the plastic would be sufficient enough to retain the timing and neutron-gamma discrimination capabilities under particular detector geometry requirements.

4.1. Detector and Data Acquisition

To investigate the timing performance of varying detector setups, coincidence time distributions and time of flight distributions between photosensors attached to opposite ends of plastic scintillators were measured. Two main types of detector setups were tested, the first being small scintillators attached to SiPMs to determine SiPM timing capabilities, and the second was bars of EJ276 coupled to small fast timing PMTs in order to determine the feasability of incorporating n-γ discriminating plastic. For both setups, the same data acquisition (DAQ) was used to record signals from the detector setup. The system utilized 16-bit, 250 MHz Pixie-16 digitizers developed by XIA LLC [18] to digitize and store traces for later high resolution timing analysis. A detailed description of a similar DAQ setup can be found in [19].

4.2. High Resolution Timing

Time-of-flight as well as position of the scintillation interaction between two photo-detectors can be determined using the time differences between the signals from each end of a length of scintillator. The internal timestamping of the XIA Pixie-16 digitizers is only in 8 ns intervals so a method to determine a more precise timing was implemented. The high resolution time of each digitized pulse was determined by means of a Polynomial Constant Fraction Discrimination algorithm (PolyCFD) [17]. The algorithm calculates the maximum from a polynomial fit around the peak of the digitized pulse and it calculates the CFD threshold as a fraction of the difference between the maximum and the baseline. The high resolution timestamp is found from a linear interpolation between the points surrounding the CFD threshold in the leading edge. The optimum threshold fraction values were obtained for a factor range between $F = 40 - 45\%$. A graphical representation of the PolyCFD method can be seen in Figure 7.

A ^{90}Sr source was employed to measure left-right position resolution because of the effective collimation due to the short range of the beta particles

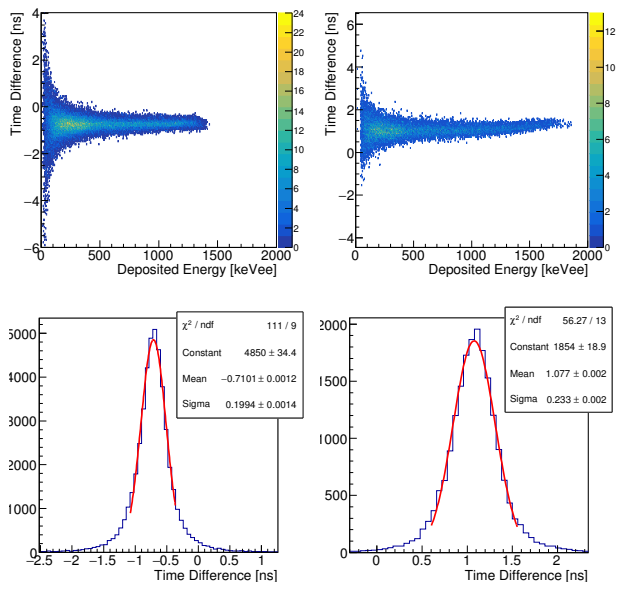

Figure 8: Top: Two-dimensional histogram of the left-right time difference versus the deposited energy in EJ-200 plastic scintillator from a ^{90}Sr source, measured with on-board amplification (left) and without it (right). Bottom: Projection on the time axis of the distributions of top panels. The red line corresponds to the gaussian fit used to determine the time resolution.

within the scintillator material. The ^{90}Sr source also provided a wide range of energy depositions from tens of keV up to ∼2 MeV. This helped establish the timing performance of different detector setups as a function of energy deposition in the scintillator. To determine time-of-flight capabalities of varying detector setups, neutrons from a readily available ^{252}Cf fission source were observed and their respective flight times were measured between START and STOP detectors. The ^{252}Cf neutron emission is very well characterized and is provides a good test of a time-of-flight detector's capabilities.

5. Timing with SiPMs

Silicon Photomultipliers (SiPMs) offer a small form factor solution to detector design and quantum efficiency uniformity for multi-detector arrays. SiPM position and time-of-flight resolution was measured to test their applicability to a small scale array. Two different readout circuits were designed for the SiPM timing measurements to measure the effects of the onboard filtering/amplification. The first one consisted of a simple low-pass active filter based on the Texas Instruments® OPA656 operational amplifier recommended by the SiPM manufacturer [20]. The feedback resistor value was chosen to be 25Ω to maintain the fast rise-time of the SiPM signal while filtering high-frequency noise. The second circuit tested does not have any onboard amplification. Pairs of the same SiPM signal readout boards were tested with a teflon-wrapped $50 \times 6 \times 6$ mm^3 piece of EJ-200 plastic scintillator between them. For each pair, the signals were amplified and gain matched using an ORTEC® 535 fast amplifier module.

5.1. SiPM Position Resolution

Figure 8 shows the results of the timing measurements using the teflon-wrapped piece of EJ-200 with the two circuits mentioned previously. The left panels correspond to the circuit with active onboard amplification and right ones the the circuit with no onboard amplification. The top panels show 2D-histograms of the left-right time difference and the deposited energy in the plastic scintillator with onboard SiPM amplification (left) and without amplification (right). The maximum of the energy distribution in the case of the SiPM circuit with amplification is lower than the one without it. This is due to the fact that signals with amplitudes larger than 1 V saturate the ADCs and were not included in the histogram. The gain of the amplifier included in the SiPM circuit boards produces the saturation at smaller energy deposition. It is also worth mentioning that the the distribution corresponding to the non amplified circuit shows a significant walk effect at high energy deposition compared to the amplified board.

Lower panels of Figure 8, show projections on the time axis of the histograms shown in the upper panel. The time resolution is obtained from gaussian fits of the time distributions. The resolutions obtained for the amplified circuit and the non-amplified one are $\Delta t = 469$ ps (FWHM), and $\Delta t = 548$ ps (FWHM) respectively.

5.2. Time of Flight with SiPMs

As a proof of principle, a small scale ToF setup (30 cm flight path) was implemented to measure neutron flight times from a ^{252}Cf source. The setup consisted of a $20 \times 6 \times 6$ mm^3 piece of EJ-200 plastic scintillator attached to 6×6 mm^2 SensL® SiPMs used as a START detector and a $100 \times 6 \times 6$ mm^3 scintillator bar attached to another pair of SensL®

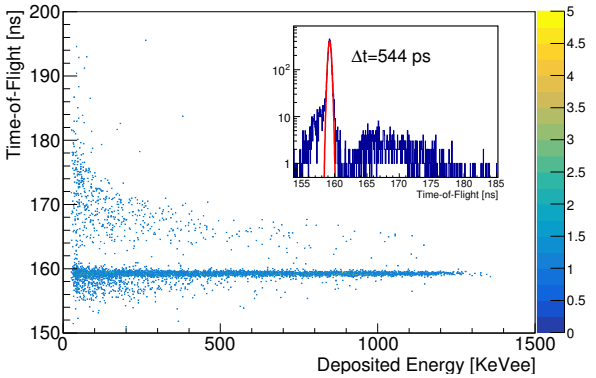

Figure 9: Two-dimensional histogram of ^{252}Cf time of flight measurements plotted against deposited energy in the EJ-200 stop detector. The inset show a logarithm projection onto the time of flight axis. The timing resolution was determined to be 544 ps from a gaussian fit to the gamma peak.

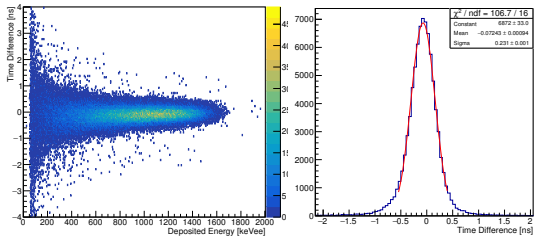

Figure 10: Left: Two-dimensional histogram of the time difference between PMTs on opposite ends of a 254 mm ESR wrapped bar of EJ-276. Right: Projection of 2D histogram on the time axis. A gaussian fit to the distribution is shown in red.

SiPMs used as the STOP detector. Both detectors were placed 30 cm apart and the same DAQ was used from the position resolution tests. A ToF vs. deposited energy distribution can be seen in Figure 9, along with a 1-D projection showing the gaussian fit to the gamma-ray peak. Using the PolyCFD method, the time of flight resolution for the SiPM setup was determined to be $\Delta t = 544$ ps (FWHM).

The small scale SiPM timing tests establish SiPMs as viable detectors for small scale arrays. Testing will continue to determine scalability of SiPMs to a large, multi-detector resistive readout system.

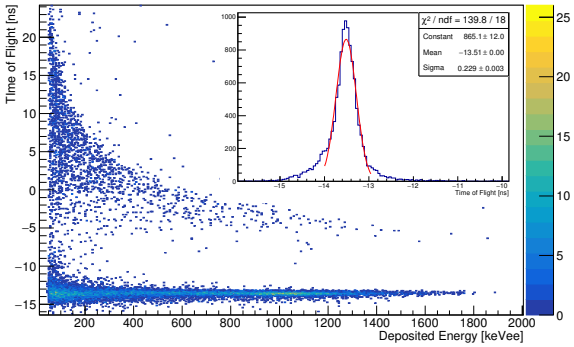

Figure 11: Two-dimensional histogram of ^{252}Cf time of flight versus deposited energy in the mylar wrapped EJ-276 stop detector. The inset is a projection of the gamma-ray peak in the time of flight spectrum and has a 538 ps FWHM [50 keVee threshold].

6. Eljen 276 Detector Tests

6.1. Timing Tests with PMTs

Timing performance of $127 \times 12.7 \times 6$ mm^3 EJ-276 bars was tested using fast, compact Hamamatsu R11265U photomultipliers. The bars of EJ-276 were machined from 12.7 mm thick sheets by Agile Technologies, Inc. and were wrapped with either 3M™ ESR (Enhanced Specular Reflector) or Lumirror™ (produced by Toray). Some bars were also provided with no wrapping to determine the effect of the reflective layers. ESR is a specular reflector with 98% reflectivity in the visible spectrum and Lumirror™ is a diffuse reflector similar to teflon. Both wrappings were applied to the EJ-276 bars using an UV-cured optical adhesive. Figure 10 shows the 2D-histogram of left-right time difference plotted against the deposited energy in the ESR-wrapped EJ-276 scintillator. The inset in Figure 10 shows the y-axis projection of the timing resolution as a gaussian distribution. From a fit to the time difference projection, the left-right timing resolution is $\Delta t = 543$ ps (FWHM). The Lumirror™ wrapped detector was not tested for timing due to the poor neutron-gamma discrimination that will explained in Section 6.2. A ToF setup similar to the SiPM test was made to measure the time of flight resolution for a single 127 mm long bar of EJ-276 plastic scintillator wrapped with ESR. Utilizing the same start detctor from the SiPM time of flight setup and the EJ-276 bar coupled to PMTS as the stop detector, the ^{252}Cf ToF spectrum was measured. From a fit to the gamma-ray peak in the

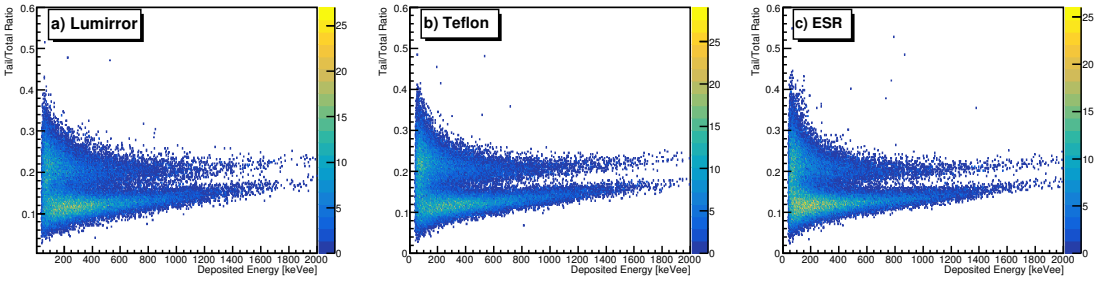

Figure 12: Two dimensional histograms of the CCM PSD for three different types of wrapping.

the time of flight spectrum, the time resolution was determined to be $\Delta t = 538$ ps [50keVee threshold applied].

6.2. neutron-γ discrimination

EJ-276 evolved from first-generation neutron-gamma discriminating plastic scintillator, EJ-299. Typical solid-state scintillators are cast or grown in specific molds, limiting detector designs. EJ-276 is capable of being cut and polished in desired geometries to optimize detector light collection. The pulse shape discrimination (PSD) response of EJ-276 is the same as EJ-299 with a slower neutron decay component than the gamma-ray response. The PSD response mechanism for EJ-299 can be found accurately described in [11]. The materials response to neutron and gamma-ray scattering was tested for the long narrow segments with different wrappings.

Two wrapped bars from Agile Technologies, Inc. (3M™ ESR and Lumirror™) and a third bare bar wrapped with teflon were tested to measure the effect of the outer reflective layer on the pulse shape discrimination. The neutron and gamma-ray responses from EJ-276 were recorded with the same 16 bit 250 MHz digitizer used for earlier setups, and the pulse shape discrimination was tested using the Charge Comparison Method [21]. By measuring the total and partial (tail) integral of each signal and calculating the ratio between the two integrals, neutrons scattering events can be separated from gamma-ray scatters. This approach is further improved by utilizing both ratios from detectors on either end of a scintillator bar and calculating the geometric mean. This method has previously been determined to be optimal when using a high bit-resolution digitizer [22]. Using the ^{252}Cf source and a 2 inch block of lead to attenuate the large gamma-ray flux, the waveforms from each bar were digitized and tail to total integral ratios were calculated. Figure 12 shows the PSD plots for bars wrapped with Lumirror™ (a), teflon (b), and ESR (c) with figure of merits being calculated between 400 and 500 keVee. The figure of merits for the Lumirror™, teflon, and ESR bars were 0.820±0.012, 1.042±0.016, and 0.977±0.015 respectively. Further tests of the bar were only done with 3M™ ESR wrapping to maintain the best neutron-gamma discrimination.

7. NEXT Prototype

ESR wrapped individual EJ-276 bars were shown to meet NEXT design goals, leading to the assembly of 2x2 in^2 segmented detectors. The prototype has 4x8 scintillator cells, the higher segmentation being along the particle flight path (see Figure 13). A full NEXT prototype is made up of one segmented array coupled to Hamamatsu H12700A position sensitive PMTs (PSPMTs) on each end of the segmented scintillator. The H12700A PSPMTs have an 8x8 segmentation (64 6x6 mm^2 anodes), each anode having an individual readout. A Vertilon PSPMT Anger Logic interface board (Model SIB064B-1018) was used to reduce the position sensitive readout from 64 individual position signals to 4 position signals, one at each corner of the SIB064B-1018 resistive network. The scintillation position is reconstructed using the weighted average of the 4 corner resistive network signals based on their respective signal integrals [23]. Figure 13 shows the reconstructed array segmentations from the Anger Logic position measurement of the PSPMTs using scintillation data from a ^{60}Co source. The PSPMT common dynode signal used for timing is connected directly to the acquistion. The scintillator cell dependent analysis calculates neutron energies on a

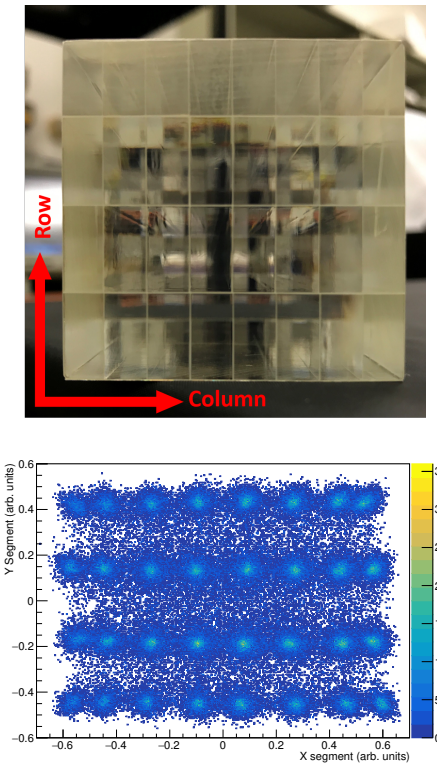

Figure 13: The top figure is an image of one end of a 4x8 segmented scintillator. The bottom figure shows the reconstructed cells using the position sensitive signals from the Vertilon Interface board. The detector is always arranged such that the 4 rows are parallel to the particle flight path and the 8 columns are perpendicular. The higher segmentation is along the flight path for the best position and timing resolution.

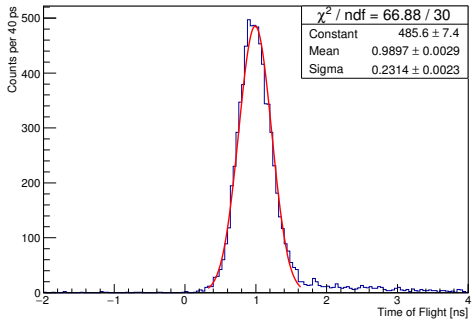

Figure 14: Time of flight resolution or a single NEXT prototype column using a collimated ^{60}Co source at a flight distance of 439.7 mm. The gaussian fit to the distribution shows the time resolution (FWHM) is 543 ps. [30 keVee threshold]

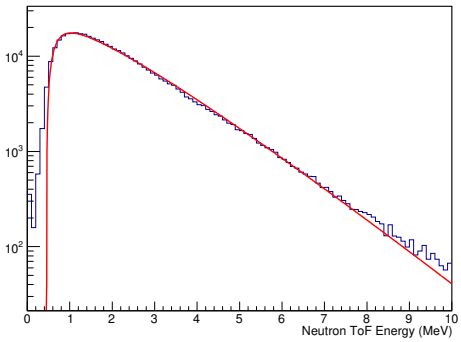

Figure 15: ^{252}Cf neutron energy spectrum as measured with the NEXT prototype using the segment dependent analysis (blue). The red line shows the expected neutron yield based on a 100 keVee detection threshold.

segment by segment basis (using reconstructed positions).

7.1. Time of Flight Measurements

To measure the prototype time of flight resolution, a collimated ^{60}Co source was used. Figure 14 shows the time of flight distribution for a single column. From a gaussian fit to the distribution, the time of flight resolution is Δt=543 ps [30 keVee threshold]. Once the prototype was established to have high resolution timing, a proof-of-principle neutron energy measurement was made using the ^{252}Cf source. The source was placed at a distance of 439.7 mm from the front face of the prototype. The neutron yield shown in Figure 15 was calculated using time-of-flight information and a neutron gate has been applied using the PSD information shown in Figure 16. The disagreement at low neutron energy is likely due to a stringent detection threshold in simulated efficiency data which was folded with the Watt equation. The standard Mannhart parameters were fixed for the Watt equation in a fit to the spectrum, with an additional scaling parameter which was floated to match the data [24].

7.2. neutron-γ discrimination

The PSPMT response is different then that of the fast timing PMTs used to initially test EJ-276. This response affects the overall pulse shape, potentially affecting the pulse shape discrimination capabilities. The dynode signals contain the pulse shape discrimination information. The four position signals lose neutron-gamma information after passing through the resistive network. Figure 16 shows the

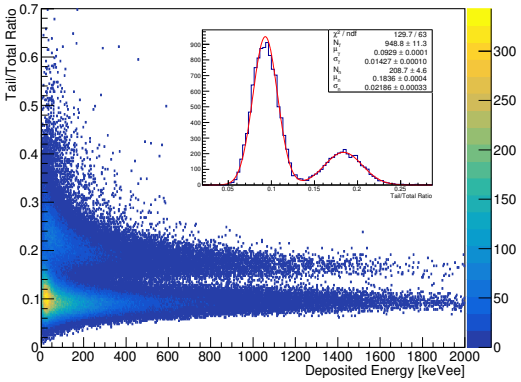

Figure 16: Neutron-gamma discrimination from the common dynode signal of the PSPMT. The walk in the distribution has been removed by correcting the gamma-ray portion to a flat line on a bin by bin basis.

neutron-gamma discrimination using the CCM. Using the same energy cuts from the wrapping tests, the FOM is 1.070±0.016. The NEXT protype does not show any noticeable effect on neutron-gamma discrimination due to segmentation or multi-anode readout.

8. Mono-Energetic Neutron Tests

NEXT's defining charactersitic is high precision, position dependent timing correlation. When neutrons pass through the segmented detector, there is a non-negligible amount of time a neutron takes to traverse the thickness of a single column. Neutron ToF measurements should therefore correspond to where within the detector the neutron interacted, e.g. neutrons that are determined to have interacted with a deeper column should have longer time-of-flights compared to those which interact in the front segments. For mono-energetic neutrons detected with the segmented NEXT prototype, the ToF distribution for each successive column should shift by the time it takes a neutron to traverse a single column thickness. In order to benchmark the timing-position correlation for the NEXT prototype, mono-energetic neutrons were measured at the Univesity of Kentucky Accelerator Laboratory (UKAL).

8.1. Experimental Setup

At UKAL, neutrons are generated in a t(p,n)^{3}He reaction, a d(d,n)^{3}He reaction, or a t(d,n)^{4}He reaction. An in-depth overview which describes the

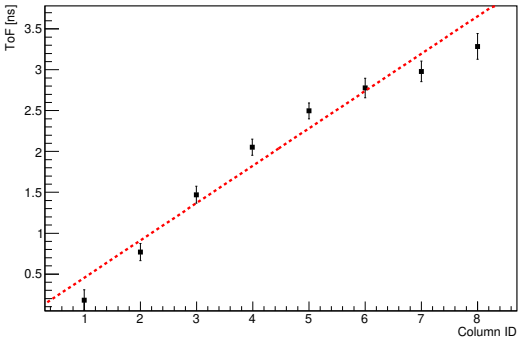

Figure 17: ToF means for each segment from simulated 1013 keV neutrons detected by the NEXT prototype using the NEXT*sim* framework. The dashed red line shows the expected position dependence of the time of flight measurements for 1013 keV neutrons.

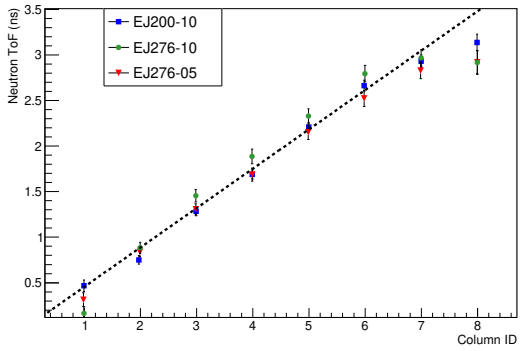

Figure 18: Plots showing the ToF shift per segment for each prototype: EJ276-10 (green), EJ276-05 (red), and EJ200-10 (blue). Data shown corresponds to time-of-flight measurements of ∼1 MeV neutrons. The data has been shifted appropriately to lie on the same scale and the associated errors are based solely on the statistical uncertainty in the determination of the mean. The black dashed line is the expected ΔToF based on neutron ToF calculations.

neutron production and energy selection of the UKAL can be found in [25]. The t(p,n)^{3}He reaction was used to generate neutron energies in the 0.248 to 1.5 MeV range, but only ∼1 MeV neutrons will be discussed below as an example of NEXT's position dependent timing characteristics. NEXT was situated behind stacked copper, polyethylene/lead, and paraffin/lithium carbonate collimators and aligned at 55° w.r.t. the proton beam direction, corresponding to 1013 keV neutrons. Due to the acceptance window of the detctor and collimators, observed neutron energies ranged from approximately 993 keV to 1035 keV. Using the same 16 bit, 250 MHz pixie-16 based acquisition system as with previous setups, neutron

time-of-flights were measured as the time difference between the proton beam pickoff signal before the tritium target and the dynode timing signals from the NEXT prototype. The specialized XIA LLC® pixie-16 firmware allowed the acquisition to be run in triple coincidence [19]. Although only one prototype was tested at a time, each detector requires 10 pixie channels, which can saturate the digitizer with a much lower count rate. The triple coincidence firmware has internal triggering that will only write a full event if the one start signal (proton beam pickoff) and the two stop signals (left-right dynode timing signals) both trigger within the pre-determined coincidence window. This helped lower triggering thresholds into electrical noise levels while still maintaining a stable, unsaturated count rate.

8.2. Simulating Time-of-Flight Propogation

Ideally, the shift in the mean of ToF distributions for each successive segment would be constant. A simulation replicating UKAL NEXT measurements was done to provide an estimate of the detector response to ∼1 MeV neutrons. 1013 keV neutrons in a pencil beam with beamspot radius 25.4 mm were simulated along a 3.1 m flight path to the front of a NEXT prototype. Only 1013 keV neutrons were simulated because the neutron energy distribution of the UKAL setup has not been fully studied. Using the full NEXT*sim* simulation (GEANT4 interactions and photosensor response), neutron ToF were measured and the mean of each segments distribution was plotted against the corresponding segment number. In order to compute the optical photon center-of-mass (segment position), the weighted average is taken of the X and Y positions of each individual photon detected at the surface of the PSPMT. Each detection event is weighted using the product of the gain of the anode which was hit and the quantum efficiency of the PSPMT for a given wavelength. In doing so, a position map similar to what is shown in Figure 13 can be made using simulated data. Figure 17 shows the expected prototype position dependent timing behavior when detecting ∼1 MeV neutrons. The dashed red line is the expected fit based on 1013 keV neutron ToF calculations. The same methods used to cut on the resistive network event position in experimental data were used for position selections from optical photon center of mass calculations in the simulated data. 1013 keV neutrons traverse a single cell thickness (6.35 mm) in 0.457 ns. The first row in Table 1 shows the shift in ToF per column (ΔToF) determined by fitting a first order polynomial to the simulated data. From the fit, ΔToF is 0.456 ns, the same as calculated, but the data is not well described with a linear fit. This could be attributed to effects of neutron scattering or scintillation light collection. Simulations were performed to investigate this effect and multi-neutron scattering effects were excluded. However, when first photon arrival time is plotted against column position, the relation is highly linear, meaning the non-linear behavior seen in Figure 17 is likely due to photon transport effects within the detector. Using NEXTsim, the prototype timing dependencies will be continually studied and fully characterized.

Table 1: Slopes ΔToF in $[^{ns}/_{col}]$ from first order polynomial fit to simulated and real ToF data for 1013 keV neutrons.

Prototype	ΔToF $\left[\frac{ns}{col}\right]$
NEXT*sim*	0.456 ± 0.020
EJ276-10	0.439 ± 0.013
EJ276-05	0.402 ± 0.013
EJ200-10	0.424 ± 0.010

8.3. Preliminary Results

To demonstrate the feasability of NEXT, a preliminary analysis was done on ∼1 MeV neutrons detected in three different segmented NEXT prototypes: EJ276-10 (10 inch EJ-276 4x8 array), EJ276-05 (5 inch EJ-276 4x8 srray) and EJ200-10 (10 inch EJ-200 4x8 array). For 1013 keV neutrons, the mean of the ToF distributions should shift by 0.432 ns for each successive column. The cell thickness is slightly less than used in the simulation due to manufacturing constraints, so the expected Δ is ∼20 ps less than was was calculated for the simulated data (0.457 ns). By making cuts for each column, the mean of each column ToF distribution was extracted using a gausian fit to 1.5σ around the maximum. ΔToF for each prototype was determined from a first order polynomial fit to the mean time-of-flight vs. column data shown in Figure 18. The ΔToF values for the fit to each prototypes are shown in Table 1. Overall, each detector showed expected position dependent timing characteristics, with a clear shift in ToF measurements from column to column. The largest difference from the expected slope was observed in the EJ276-05

prototype. Column 8 consistently had a smaller shift in ToF possibly due to improper position selection due to low statistics for this column or as a physical effect of the detector. Continuing analysis on this data set will be performed along with other ToF data acquired for different neutron energies.

9. Conclusions

After extensive development guided by simulations and single segment tests, a NEXT prototype has been built with 4x8 segmentation. The prototype meets design goals with 6 mm tile thickness and 548 ps time-of-flight resolution. A proof-of-principle neutron energy measurement was made using fission neutrons from a ^{252}Cf source. The measured neutron yield matched the expected distribution based on GEANT4 prototype simulations. Also, the position dependent timing was evaluated through preliminary analysis of 1013 keV neutron ToF measurements using the NEXT prototypes. SensL™ J-Series SiPMs successfully measured gamma-ray time of flight with approximately 500 ps timing resolution, validating SiPMs as potential detectors for future development of small scale time of flight arrays. While NEXT is still in the prototyping phase, it will be continually redesigned to incorporate further breakthroughs in neutron-gamma discriminating solid-state scintillators and position sensitive photodetector technologies.

This research was sponsored by the U.S. Department of Energy, National Nuclear Security Administration under the Stewardship Science Academic Alliances program through DOE Award No. DOE DE-NA0002934 and DE-NA0002132.

References

References

[1] A. Gade, C. K. Gelbke, T. Glasmacher, Nucl. Phys. News 24 (1) (2014) 28.

[2] M. Pfützner, M. Karny, L. V. Grigorenko, K. Riisager, Radioactive decays at limits of nuclear stability, Rev. Mod. Phys. 84 (2012) 567–619. doi:10.1103/RevModPhys.84.567.

[3] T. Nakamura, H. Sakurai, H. Watanabe, Exotic nuclei explored at in-flight separators, Progress in Particle and Nuclear Physics 97 (2017) 53 – 122. doi:https://doi.org/10.1016/j.ppnp.2017.05.001.

[4] B. Blank, M. Borge, Nuclear structure at the proton drip line: Advances with nuclear decay studies, Progress in Particle and Nuclear Physics 60 (2) (2008) 403 – 483. doi:https://doi.org/10.1016/j.ppnp.2007.12.001.

[5] M. Febbraro, D. Walter, K. Chipps, S. Pain, E. Temanson, R. Toomey, A. Atencio, C. Thornsberry, K. Smith, J. ONeill, K. Jones, C. Havener, Development of an array of liquid-scintillator-based bar detectors: Sabre, Nuclear Instruments and Methods in Physics Research Section A: Accelerators, Spectrometers, Detectors and Associated Equipment 908 (2018) 189 – 197. doi:https://doi.org/10.1016/j.nima.2018.08.051.

[6] N. Kornilov, I. Fabry, S. Oberstedt, F.-J. Hambsch, Total characterization of neutron detectors with a 252cf source and a new light output determination, Nuclear Instruments and Methods in Physics Research Section A: Accelerators, Spectrometers, Detectors and Associated Equipment 599 (2) (2009) 226 – 233.

[7] W. Peters, S. Ilyushkin, M. Madurga, C. Matei, S. Paulauskas, R. Grzywacz, D. Bardayan, C. Brune, J. Allen, J. Allen, Z. Bergstrom, J. Blackmon, N. Brewer, J. Cizewski, P. Copp, M. Howard, R. Ikeyama, R. Kozub, B. Manning, T. Massey, M. Matos, E. Merino, P. O'Malley, F. Raiola, C. Reingold, F. Sarazin, I. Spassova, S. Taylor, D. Walter, Performance of the versatile array of neutron detectors at low energy (VANDLE), Nuclear Instruments and Methods in Physics Research Section A: Accelerators, Spectrometers, Detectors and Associated Equipment 836 (2016) 122 – 133.

[8] A. Buţă, T. Martin, C. Timiş, N. Achouri, J. Angélique, C. Borcea, I. Cruceru, A. Genoux-Lubain, S. Grévy, M. Lewitowicz, E. Liénard, F. Marqués, F. Negoiţă, F. de Oliveira, N. Orr, J. Péter, M. Sandu, Tonnerre: an array for delayed-neutron decay spectroscopy, Nuclear Instruments and Methods in Physics Research Section A: Accelerators, Spectrometers, Detectors and Associated Equipment 455 (2) (2000) 412 – 423. doi:https://doi.org/10.1016/S0168-9002(00)00510-6.

[9] D. Morrissey, K. McDonald, D. Bazin, B. Brown, R. Harkewicz, N. Orr, B. Sherrill, G. Souliotis, M. Steiner, J. Winger, S. Yennello, B. Young, S. Lukyanov, G. Chubarian, Y. Oganessian, Single neutron emission following 11li i^2-decay, Nuclear Physics A 627 (2) (1997) 222 – 238. doi:https://doi.org/10.1016/S0375-9474(97)00410-7.

[10] G. Perdikakis, M. Sasano, S. M. Austin, D. Bazin, C. Caesar, S. Cannon, J. Deaven, H. Doster, C. Guess, G. Hitt, J. Marks, R. Meharchand, D. Nguyen, D. Peterman, A. Prinke, M. Scott, Y. Shimbara, K. Thorne, L. Valdez, R. Zegers, Lenda: A low energy neutron detector array for experiments with radioactive beams in inverse kinematics, Nuclear Instruments and Methods in Physics Research Section A: Accelerators, Spectrometers, Detectors and Associated Equipment 686 (2012) 117 – 124. doi:https://doi.org/10.1016/j.nima.2012.05.076.

[11] N. Zaitseva, B. Rupert, I. Paweczak, A. Glenn, H. Paul Martinez, L. Carman, M. Faust, N. Cherepy, S. Payne, Plastic scintillators with efficient neutron/gamma pulse shape discrimination, Nuclear Instruments and Methods in Physics Research Section A: Accelerators, Spectrometers, Detectors and Associated Equipment 668 (2012) 8893. doi:10.1016/j.nima.2011.11.071.

[12] N. Zaitseva, A. Glenn, A. Mabe, M. Carman, C. Hurlbut, J. Inman, S. Payne, Recent developments in plastic

scintillators with pulse shape discrimination, Nuclear Instruments and Methods in Physics Research Section A: Accelerators, Spectrometers, Detectors and Associated Equipment 889 (2018) 97 – 104. doi:https://doi.org/10.1016/j.nima.2018.01.093.

[13] S. Agostinelli, J. Allison, K. Amako, J. Apostolakis, H. Araujo, P. Arce, M. Asai, D. Axen, S. Banerjee, G. Barrand, F. Behner, L. Bellagamba, J. Boudreau, L. Broglia, A. Brunengo, H. Burkhardt, S. Chauvie, J. Chuma, R. Chytracek, G. Cooperman, G. Cosmo, P. Degtyarenko, A. Dell'Acqua, G. Depaola, D. Dietrich, R. Enami, A. Feliciello, C. Ferguson, H. Fesefeldt, G. Folger, F. Foppiano, A. Forti, S. Garelli, S. Giani, R. Giannitrapani, D. Gibin, J. G. Cadenas, I. González, G. G. Abril, G. Greeniaus, W. Greiner, V. Grichine, A. Grossheim, S. Guatelli, P. Gumplinger, R. Hamatsu, K. Hashimoto, H. Hasui, A. Heikkinen, A. Howard, V. Ivanchenko, A. Johnson, F. Jones, J. Kallenbach, N. Kanaya, M. Kawabata, Y. Kawabata, M. Kawaguti, S. Kelner, P. Kent, A. Kimura, T. Kodama, R. Kokoulin, M. Kossov, H. Kurashige, E. Lamanna, T. Lampén, V. Lara, V. Lefebure, F. Lei, M. Liendl, W. Lockman, F. Longo, S. Magni, M. Maire, E. Medernach, K. Minamimoto, P. M. de Freitas, Y. Morita, K. Murakami, M. Nagamatu, R. Nartallo, P. Nieminen, T. Nishimura, K. Ohtsubo, M. Okamura, S. O'Neale, Y. Oohata, K. Paech, J. Perl, A. Pfeiffer, M. Pia, F. Ranjard, A. Rybin, S. Sadilov, E. D. Salvo, G. Santin, T. Sasaki, N. Savvas, Y. Sawada, S. Scherer, S. Sei, V. Sirotenko, D. Smith, N. Starkov, H. Stoecker, J. Sulkimo, M. Takahata, S. Tanaka, E. Tcherniaev, E. S. Tehrani, M. Tropeano, P. Truscott, H. Uno, L. Urban, P. Urban, M. Verderi, A. Walkden, W. Wander, H. Weber, J. Wellisch, T. Wenaus, D. Williams, D. Wright, T. Yamada, H. Yoshida, D. Zschiesche, Geant4—a simulation toolkit, Nuclear Instruments and Methods in Physics Research Section A: Accelerators, Spectrometers, Detectors and Associated Equipment 506 (3) (2003) 250 – 303.

[14] J. Allison, K. Amako, J. Apostolakis, P. Arce, M. Asai, T. Aso, E. Bagli, A. Bagulya, S. Banerjee, G. Barrand, B. Beck, A. Bogdanov, D. Brandt, J. Brown, H. Burkhardt, P. Canal, D. Cano-Ott, S. Chauvie, K. Cho, G. Cirrone, G. Cooperman, M. Cortés-Giraldo, G. Cosmo, G. Cuttone, G. Depaola, L. Desorgher, X. Dong, A. Dotti, V. Elvira, G. Folger, Z. Francis, A. Galoyan, L. Garnier, M. Gayer, K. Genser, V. Grichine, S. Guatelli, P. Guèye, P. Gumplinger, A. Howard, I. Hřivnáčová, S. Hwang, S. Incerti, A. Ivanchenko, V. Ivanchenko, F. Jones, S. Jun, P. Kaitaniemi, N. Karakatsanis, M. Karamitros, M. Kelsey, A. Kimura, T. Koi, H. Kurashige, A. Lechner, S. Lee, F. Longo, M. Maire, D. Mancusi, A. Mantero, E. Mendoza, B. Morgan, K. Murakami, T. Nikitina, L. Pandola, P. Paprocki, J. Perl, I. Petrović, M. Pia, W. Pokorski, J. Quesada, M. Raine, M. Reis, A. Ribon, A. R. Fira, F. Romano, G. Russo, G. Santin, T. Sasaki, D. Sawkey, J. Shin, I. Strakovsky, A. Taborda, S. Tanaka, B. Tomé, T. Toshito, H. Tran, P. Truscott, L. Urban, V. Uzhinsky, J. Verbeke, M. Verderi, B. Wendt, H. Wenzel, D. Wright, D. Wright, T. Yamashita, J. Yarba, H. Yoshida, Recent developments in geant4, Nuclear Instruments and Methods in Physics Research Section A: Accelerators, Spectrometers, Detectors and Associated Equipment 835 (2016) 186 – 225. doi:https://doi.org/10.1016/j.nima.2016.06.125.
URL http://www.sciencedirect.com/science/article/pii/S0168900216306957

[15] J. Apostolakis, G. Folger, V. Grichine, A. Heikkinen, A. Howard, V. Ivanchenko, P. Kaitaniemi, T. Koi, M. Kosov, J. M. Quesada, A. Ribon, V. Uzhinskiy, D. Wright, Progress in hadronic physics modelling in geant4, Journal of Physics: Conference Series 160 (1) (2009) 012073.
URL http://stacks.iop.org/1742-6596/160/i=1/a=012073

[16] W.-S. Choong, Phys. Med. Biol. 54 (21) (2009) 6495. [link].
URL http://stacks.iop.org/0031-9155/54/i=21/a=004

[17] C. R. Thornsberry, Ph.D. thesis, University of Tennessee (2018).

[18] XIA LLC, 31057 Genstard Rd., Hayward, CA.
URL www.xia.com

[19] S. Paulauskas, M. Madurga, R. Grzywacz, D. Miller, S. Padgett, H. Tan, A digital data acquisition framework for the versatile array of neutron detectors at low energy (vandle), Nuclear Instruments and Methods in Physics Research Section A: Accelerators, Spectrometers, Detectors and Associated Equipment 737 (2014) 22 – 28. doi:https://doi.org/10.1016/j.nima.2013.11.028.

[20] SensL, JSeries, High PDE and Timing Resolution, TSV package, User Manual.

[21] G. Ranucci, An analytical approach to the evaluation of the pulse shape discrimination properties of scintillators, Nucl. Inst. Meth. A 354 (1995) 389–399.

[22] M. Flaska, M. Faisal, D. D. Wentzloff, S. A. Pozzi, Influence of sampling properties of fast-waveform digitizers on neutrongamma-ray, pulse-shape discrimination for organic scintillation detectors, Nuclear Instruments and Methods in Physics Research Section A: Accelerators, Spectrometers, Detectors and Associated Equipment 729 (2013) 456 – 462. doi:https://doi.org/10.1016/j.nima.2013.07.008.

[23] H. Anger, Scintillation camera with multichannel collimators, J. Nucl. Med. 5 (1964) 515 – 531.

[24] W. Mannhart, Status of the cf-252 fission neutron spectrum evaluation with regard to recent experiments, in: INDC(NDS) 220, pp. 305 – 336.

[25] J. Hartman, A. Barzilov, E. Peters, S. Yates, Measurements of response functions of ej-299-33a plastic scintillator for fast neutrons, Nuclear Instruments and Methods in Physics Research Section A: Accelerators, Spectrometers, Detectors and Associated Equipment 804 (2015) 137 – 143. doi:https://doi.org/10.1016/j.nima.2015.09.068.